ACS APPLIED MATERIALS & INTERFACES

Research Article

Cite This: ACS Appl. Mater. Interfaces XXXX, XXX, XXX−XXX

www.acsami.org

Decoration of Porous Silicon with Gold Nanoparticles via Layer-by-Layer Nanoassembly for Interferometric and Hybrid Photonic/Plasmonic (Bio)sensing

Stefano Mariani,[†] Alessandro Paghi,[†] Antonino A. La Mattina,[†] Aline Debrassi,[‡] Lars Dähne,[‡] and Giuseppe Barillaro*[,†]

[†]Dipartimento di Ingegneria dell'Informazione, Università di Pisa, Via G. Caruso 16, 56122 Pisa, Italy

[‡]Surflay Nanotec GmbH, Max-Planck-Straße 3, 12489 Berlin, Germany

Supporting Information

ABSTRACT: Gold nanoparticle layers (AuNPLs) enable the coupling of morphological, optical, and electrical properties of gold nanoparticles (AuNPs) with tailored and specific surface topography, making them exploitable in many bioapplications (e.g., biosensing, drug delivery, and photothermal therapy). Herein, we report the formation of AuNPLs on porous silicon (PSi) interferometers and distributed Bragg reflectors (DBRs) for (bio)sensing applications via layer-by-layer (LbL) nanoassembling of a positively charged polyelectrolyte, namely, poly(allylamine hydrochloride) (PAH), and negatively charged citrate-capped AuNPs. Decoration of PSi interferometers with AuNPLs enhances the Fabry−Pérot fringe contrast due to increased surface reflectivity, resulting in an augmented sensitivity for both bulk and surface refractive index sensing, namely, about 4.5-fold using NaCl aqueous solutions to infiltrate the pores and 2.6-fold for unspecific bovine serum albumin (BSA) adsorption on the pore surface, respectively. Sensitivity enhancing, about 2.5-fold, is also confirmed for affinity and selective biosensing of streptavidin using a biotinylated polymer, namely, negatively charged poly(methacrylic acid) (b-PMAA). Further, decoration of PSi DBR with AuNPLs envisages building up a hybrid photonic/plasmonic optical sensing platform. Both photonic (DBR stop-band) and plasmonic (localized surface plasmon resonance, LSPR) peaks of the hybrid structure are sensitive to changes of bulk (using glucose aqueous solutions) and surface (due to BSA unspecific adsorption) refractive index. To the best of our knowledge, this is the first report about the formation of AuNPLs via LbL nanoassembly on PSi for (i) the enhancing of the interferometric performance in (bio)sensing applications and (ii) the building up of hybrid photonic/plasmonic platforms for sensing and perspective biosensing applications.

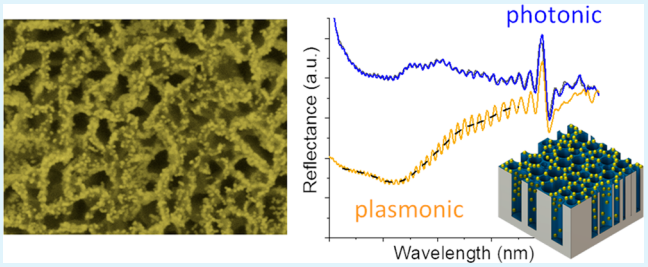

KEYWORDS: *gold nanoparticles (AuNPs), porous silicon (PSi), layer-by-layer (LbL) nanoassembly, interferometer, distribute Bragg reflector (DBR), hybrid photonic/plasmonic, sensor, biosensor*

INTRODUCTION

Gold nanoparticle layers (AuNPLs) refer to 2-D surfaces with immobilized gold nanoparticles (AuNPs) (arrays of thin film) on a substrate (polymer, glass, or metal).[1] AuNPLs enable coupling the properties of AuNPs (e.g., high surface/volume ratio, electrical and optical properties, and basic biochemical modification) with a tailored and specific surface topography.[1] This makes AuNPLs suitable for many bioapplications ranging from biosensing (optical, e.g. (localized) surface plasmon resonance ((L)SPR),[2,3] surface enhanced Raman scattering (SERS),[4−6] enzyme-linked immunosorbent assay (ELISA),[7−9] and electrochemical[10]) to drug delivery, from photothermal therapy[1,11] to antibacterial surface.[1]

Two different methods have been mostly used to fabricate AuNPLs: (i) in situ reduction of tetrachloroauric acid ($HAuCl_4$) solution for the growth of AuNPs directly onto the target surface or (ii) self-assembling of previously synthesized AuNPs on the target substrate.[1,11] The in situ reduction is usually achieved by (i) spontaneous reduction of $HAuCl_4$ on the surface of reducing material (e.g., silicon);[1] (ii) use of reducing agents to promote reduction of $HAuCl_4$;[12] and (iii) electrodeposition of gold on the target material in an electrochemical cell.[13] A chief advantage of self-assembling of AuNPs onto the target surface, compared to in situ reduction, is that AuNPs' properties (i.e., shape, dimension, coating, and related optical and electrical features) can be finely tuned during their synthesis, i.e., before their assembling. The assembling is usually achieved by either covalent or noncovalent chemistry. As to noncovalent chemistry, the employment of electrostatic interaction between charged polyelectrolytes and charged AuNPs, for instance, using layer-by-layer (LbL) nanoassembly, offers a good control of the layer

Received: August 31, 2019
Accepted: October 23, 2019
Published: October 23, 2019

DOI: 10.1021/acsami.9b15737
ACS Appl. Mater. Interfaces XXXX, XXX, XXX−XXX

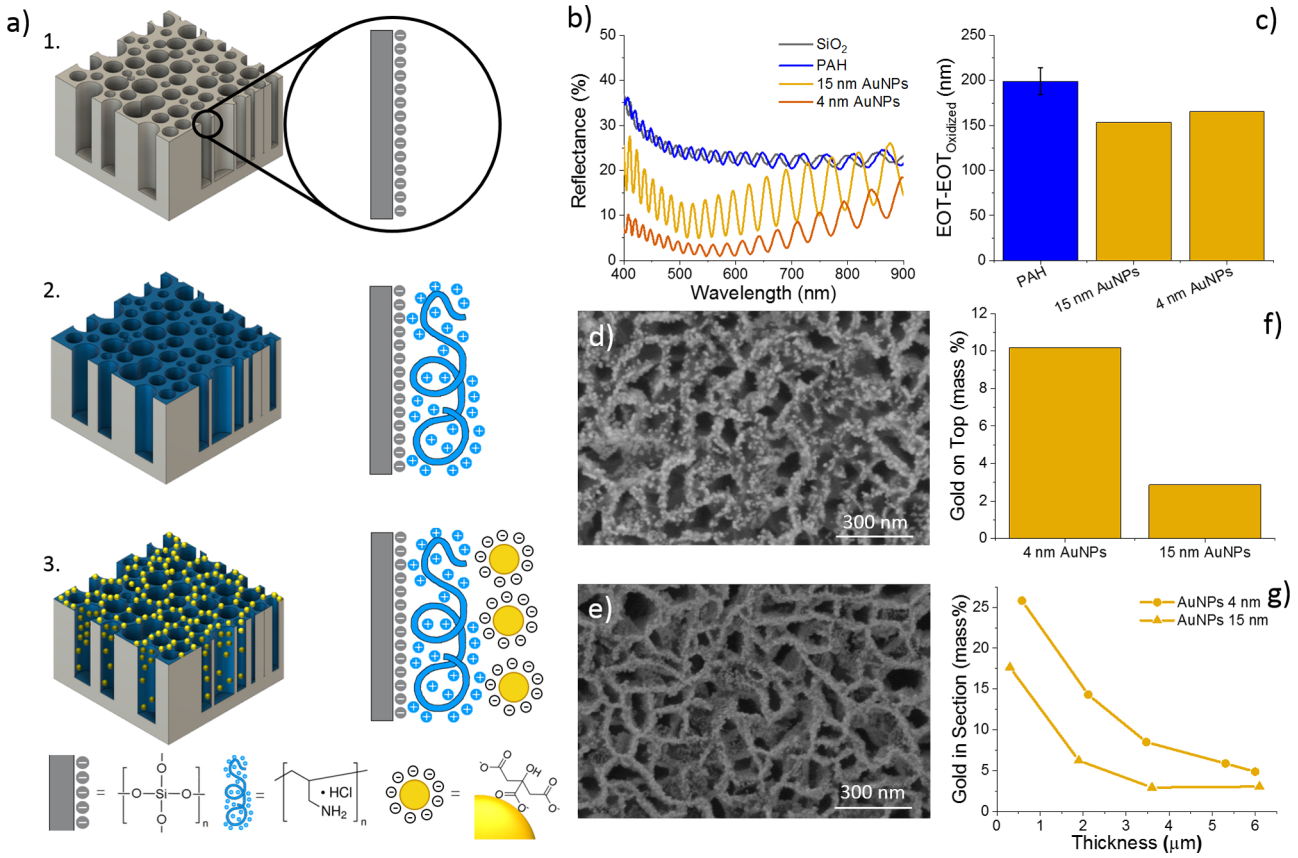

Figure 1. Fabrication and characterization of AuNPs-decorated PSi interferometers. (a) Sketch of the process steps for AuNP decoration of PSi interferometers via LbL nanoassembly: (1) preparation and oxidation of PSi interferometers (gray, negatively charged); (2) PAH coating (blue, positively charged) of oxidized PSi interferometers; (3) AuNP decoration (yellow, negatively charged citrate-capped) of PAH-coated PSi interferometers. (b) Reflectance spectra recorded in air of PSi interferometers after oxidation, PAH coating, and decoration with 15 and 4 nm sized AuNPs. (c) EOT − EOT_{ox} value of oxidized PSi interferometers after assembling of PAH (blue bar) and after decoration with 15 and 4 nm sized AuNPs (yellow bars). (d, e) Top-view SEM images of oxidized PSi interferometers decorated with 15 and 4 nm sized AuNPs, respectively. (f, g) Au mass percentages on top and over depth of oxidized PSi interferometers decorated with 15 and 4 nm sized AuNPs.

thickness at nanoscale level with respect to other thin-film deposition methods, especially for micro- and nanostructured surfaces.[14−16]

The electrostatic LbL nanoassembling of polyelectrolytes and AuNPs has been successfully reported exploiting charged nanoparticles. Most of the synthesis protocols of AuNPs involve the use of capping/reducing agents to maintain the AuNP surface covered with a net charge that is functional to the formation of a colloidal dispersion via electrostatic repulsion.[1,17] Budy et al. reported charged polymer-mediated LbL assembly of gold nanoparticles with different shapes (i.e., spherical, rod, triangular, prismatic, and octahedral) on a glass substrate.[17] The nanoparticles capped with negatively charged (e.g., citrate) or positively charged (e.g., phosphatidylcholine, cetyltrimethylammonium bromide, and polydiallyldimethylammonium chloride) agents were assembled with cationic (poly(diallyldimethylammonium chloride) and polyethylenimine) or anionic (poly(sodium 4-styrenesulfonate)) polyelectrolytes on glass slides for optical refractive index sensing using LSPR.[17]

Among the different state-of-the-art platforms for optical (bio)sensing, nanostructured porous silicon (PSi) offers a number of peculiar advantages, such as high surface area (hundreds of m^2/g) and tunable optical properties (e.g., interferometers,[18,19] distributed Bragg reflectors (DBRs),[20,21] rugate filters,[22,23] and resonant microcavities have been reported).[24,25] PSi has been successfully used over the past 20 years for refractive index sensing,[18,19] gas/vapor sensing,[26−31] and label-free biosensing.[32−37] Hybrid platforms using PSi as a host matrix for several nanomaterials, such as, polymers, metals, quantum dots (QDs), fluorescent molecules, graphene oxide (GO), carbon nanotubes (CNTs), and carbon dots (C-dots), have also been proposed.[32] The main advantage of PSi-based hybrid platforms is related to their superior sensing performance compared to the individual components, in terms of, dual-mode detection, signal enhancement, higher sensitivity, and improved signal stability.[32] As to decoration of PSi with metal nanoparticles (e.g., AuNPs), this was mainly investigated for SERS applications,[38] in which PSi did not significantly contribute to the optical signal transduction, serving only as support matrix for the in situ direct reduction of the metal nanostructures on the PSi surface.[39]

Herein, we report on the formation of controlled AuNPLs on PSi interferometers and DBRs via LbL nanoassembling of a positively charged polyelectrolyte, namely, poly(allylamine hydrochloride) (PAH), and negatively charged citrate-capped AuNPs, which were synthesized according to the Turkevich[40,41] method or by chemical reduction.[42]

Decoration of PSi interferometers with AuNPLs enhances the Fabry−Pérot fringe contrast due to augmented surface reflectivity,[43] resulting in an increased sensitivity for both bulk refractive index sensing (about 4.5-fold) and unspecific/affinity

DOI: 10.1021/acsami.9b15737
ACS Appl. Mater. Interfaces XXXX, XXX, XXX−XXX

biosensing (about 2.5-fold). Further, we show that decoration of PSi DBR with AuNPLs can be exploited for building up hybrid photonic/plasmonic optical sensing platforms. In fact, both photonic (DBR stop-band) and plasmonic (LSPR) peaks were sensitive to changes of bulk and surface refractive index, upon infiltration of the pores with glucose solutions or BSA adsorption on the pore surface, respectively.

To the best of our knowledge, this is the first report about the formation of AuNPLs via LbL nanoassembly on porous silicon for enhancing the interferometric sensitivity in (bio)-sensing and for the building of photonic/plasmonic hybrid platforms for perspective (bio)sensing applications.

RESULTS AND DISCUSSION

Decoration of PSi Interferometers with AuNPs via LbL Nanoassembly. Electrostatic decoration of porous silicon interferometers with AuNPs was carried out as depicted in Figure 1a, according to the procedure described in AuNPs-Decoration of Porous Silicon Interferometers and DBRs via Layer-by-Layer Nanoassembly (Experimental Section). Thickness (4.97 ± 0.06 μm, five samples) and porosity (79.8 ± 1.5%) of as-prepared PSi layers were estimated through analysis of the reflectance spectrum.[30] As-prepared PSi layers were thermally oxidized (Figure 1a(1)) to convert silicon to silicon dioxide and provide the PSi surface with a net negative charge. The oxidation also enhances hydrophilicity and chemical stability of PSi layers in water.[44] A positively charged polymer, namely, PAH, was next assembled onto the negatively charged surface of oxidized PSi layers by drop-casting of a PAH solution (Figure 1a(2)). Eventually, decoration of PAH-coated PSi layers with AuNPs was achieved by drop-casting of a solution of negatively charged citrate-capped AuNPs, either with larger size of 15 nm (concentration, 2.89×10^{-9} M) or with smaller size of 4 nm (concentration, 4.20×10^{-7} M) (Figure 1a(3)).

Effective optical thickness (EOT) values achieved through fast Fourier transform (FFT) of reflectance spectra acquired in air (Figure 1b and Supporting Information Figure S1) were used to infer the successful achievement of each of the preparation steps. The EOT value of as-prepared PSi interferometers (EOT_0 = (1.456 ± 0.037) × 10^4 nm) decreased after thermal oxidation ($EOT_{ox} - EOT_0$ = (−1.43 ± 0.23) × 10^3 nm) due to the lower refractive index of silicon dioxide (1.460 RIU, at 550 nm),[45] compared to that of silicon (4.087 RIU, at 550 nm).[46] Coating of oxidized PSi interferometers with PAH led to an increase of the EOT value, namely, $EOT_{PAH} - EOT_{ox}$ = 203 ± 14 nm (Figure 1c). The EOT value decreased again after decoration of PAH-coated PSi layers with AuNPs, namely, $EOT_{AuNPs} - EOT_{ox}$ = 153 and 166 nm with 15 and 4 nm AuNPs, respectively (Figure 1c). Figure S1c,d reports normalized FFT amplitude spectra achieved from PSi reflectance spectra acquired before and after decoration with AuNPs. The increase/decrease of EOT after PAH and AuNPs coating agrees with the higher/lower refractive index of PAH (1.468 RIU, at 550 nm)[47] and gold (0.434 RIU for 15 nm,[48] and 0.763 RIU for 4 nm, at 550 nm[49]), compared to that of air (1.000 RIU),[50] in the spectral range under investigation. The effective refractive index (n_{eff}) values achieved from EOT data on PSi layers with average thickness of 4.97 μm resulted in 1.465 RIU for as-prepared samples, 1.321 RIU after oxidation, 1.341 RIU after PAH coating, and roughly 1.336 RIU after decoration with both AuNPs of 15 and 4 nm.

For both AuNP sizes, an increase of the interferometric Fabry−Pérot fringe contrast in the experimental reflectance spectra (Figure 1b), and, thus, of the amplitude of the FFT spectra (Figure S1c,d), was achieved (~3.3 fold for 15 nm sized AuNPs and ~1.2 fold for 4 nm sized AuNPs). Such an increase was ascribed to an augmented reflectivity of the top surface of PSi interferometers upon slight metallization with AuNPs (i.e., mirroring effect).[43] Theoretical reflectance spectra (Figure S2) of PSi interferometers calculated with the transfer matrix method (TMM) and taking into account AuNP coverage of only the top surface clearly supported this hypothesis, once the fringe mean amplitude was evaluated. Specifically, a hexagonally arranged layer of Au nanoparticles on top of the oxidized PSi interferometer skeleton was considered. Increasing the diameter of AuNPs (i.e., the gold thickness) initially led to an increase of the fringe amplitude in the theoretical reflectance spectrum, due to an enhanced reflection at the top surface of PSi interferometers, until a maximum value was reached for a diameter around 30 nm; beyond this diameter/thickness value, gold absorption played an important role and hindered light propagation in the underlying PSi structure, thus leading to a decrease of the fringe amplitude in the theoretical reflectance spectrum. Notice that, theoretical calculations highlight that the AuNP layer assembled on top of the PSi interferometer does not produce any significant plasmonic effect.

Furthermore, the experimental reflectance spectra of PSi interferometers decorated with 15 and 4 nm sized AuNPs showed a decrease of the reflectance value in the range 400−600 nm, which was ascribed to LSPR absorption of AuNPs decorating the inner surface of the nanopores over depth (see the LSPR spectrum of AuNPs in aqueous dispersion reported in Figure S3). The widening of the LPSR region in the reflectance spectra of AuNPs-coated PSi interferometers, with respect to the AuNP LSPR peak profile in aqueous dispersion (Figure S3), can be explained in terms of aggregation of the nanoparticles on the PSi surface upon drying.[51]

Panels (d) and (e) of Figure 1 show top-view scanning electron microscope (SEM) images of PSi interferometers decorated with 15 and 4 nm AuNPs, respectively. More in detail, AuNPs with a size of 4 nm decorated the PSi scaffold with higher density compared to AuNPs with a size of 15 nm. This is semiquantitatively corroborated by SEM-EDS (energy-dispersive X-ray spectroscopy) analysis of both top and cross-section of the PSi interferometers after AuNP decoration (Figure 1f,g). The EDS analysis of the top surface of AuNPs-decorated PSi structures resulted in an Au mass of 2.86 and 10.18% for larger and smaller NPs, respectively (Figure 1f). Further, EDS analysis of the cross-section revealed that 15 nm sized AuNPs poorly penetrated the inner surface of PSi interferometers, with an Au mass within the first 500 nm from the top surface of 17.65%, rapidly decaying to 6.24% at a depth of 1.5 μm and reaching a baseline value of 2.93% at a depth of 3 μm (Figure 1g); conversely, the 4 nm sized AuNPs efficiently decorated the inner surface of PSi interferometers throughout the whole thickness, with an Au mass of about 25% within the first 500 nm from top, decreasing with depth down to roughly 10% at ~3 μm (Figure 1g). The decreased AuNP concentration with depth well agrees with the model reported by Chen and Sailor[52] about infiltration and adsorption of charged molecules inside a PSi layer. Indeed, after adsorption on the PAH-coated nanopore surface, the negative surface

DOI: 10.1021/acsami.9b15737
ACS Appl. Mater. Interfaces XXXX, XXX, XXX−XXX

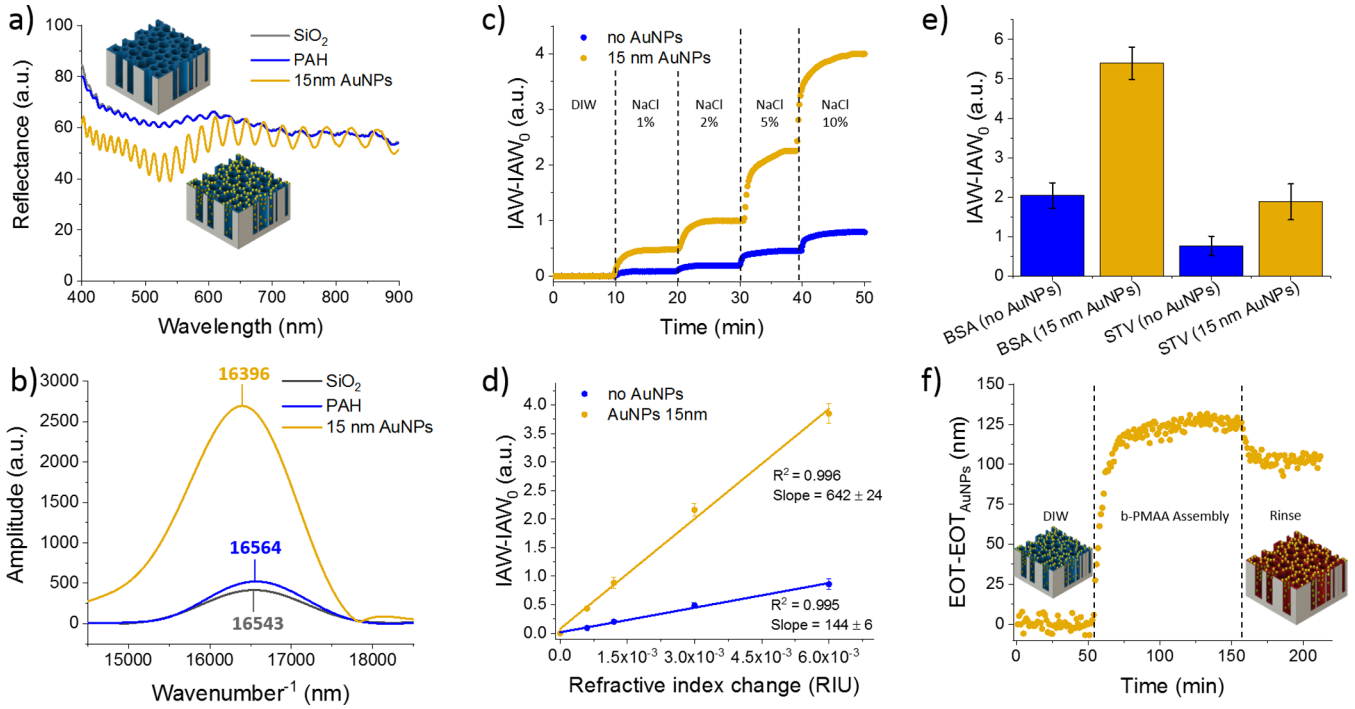

Figure 2. AuNPs-decorated PSi interferometer (bio)sensing characterization. (a) Reflectance spectra of an oxidized PSi interferometer acquired in DIW, before (gray) and after (blue) PAH coating and after decoration with 15 nm sized AuNPs (yellow). (b) Representative Fourier transform amplitude of the reflectance spectra in panel (a). (c) Sensorgram IAW − IAW_0 vs time acquired during injections of NaCl solutions (1, 2, 5, and 10%) on nondecorated and AuNPs-decorated PSi interferometers. (d) Calibration curve IAW − IAW_0 vs refractive index variations (with respect to DIW) obtained from the sensorgrams in panel (c). (e) IAW − IAW_0 signals of BSA unspecific adsorption and STV selective binding measured on nondecorated (blue bars) and decorated (yellow bars) PSi interferometers. (f) EOT − EOT_{AuNPs} value vs time acquired during the assembly of biotinylated PMAA (b-PMAA) on a AuNPs-decorated PSi interferometer. Data in panels (d) and (e) are provided as average values over three replicates, with error bars representing one standard deviation.

charge of AuNPs (due to citrate-capping) generates electrostatic repulsion forces restricting diffusion of further AuNPs inside the nanopores as the depth increases.

Plasmonic absorption of AuNPs-infiltrated PSi interferometers is confirmed by theoretical spectra (Figure S2c,d) calculated with TMM and taking into account gold nanoparticle decoration of only the inner nanopore surface of PSi interferometers (i.e., no AuNPs on the top surface), with a concentration profile over depth reflecting that achieved by SEM-EDS measurements. Specifically, for 15 nm sized AuNPs, aconcentration profile (given as percentage of the PSi layer volume) decaying with depth from 0.67% (top) to 0.16% at 2.5 μm, and then with constant value of 0.07% down to the bottom was considered; for 4 nm sized AuNPs, a concentration profile decaying from 0.85% (top) to 0.18% (bottom) was used.

(Bio)sensing with AuNPs-Decorated PSi Interferometers. The analytical performance of AuNPs-decorated PSi interferometers for (bio)sensing purposes were evaluated by interferogram average over wavelength (IAW) reflectance spectroscopy.[53] The IAW value was calculated as the average value of the spectral interferogram resulting upon subtraction of the reflectance spectrum recorded after injection/adsorption of the target analyte and the reference reflectance spectrum recorded in bare buffer. The increased Fabry−Pérot fringe contrast achieved through decoration of PSi interferometers with AuNPs was expected to improve the analytical performances of PSi interferometers in terms of sensitivity for (bio)sensing. Thus, PSi interferometers decorated with 15 nm AuNPs were selected as a case study due to their enhanced Fabry−Pérot fringe contrast with respect to those with 4 nm AuNPs.

Oxidized PSi interferometers were placed in a flow cell, then coated with PAH and decorated with AuNPs (directly in the flow cell, to avoid drying steps and, in turn, NP aggregation). The protocol is described in AuNPs-Decoration of Porous Silicon Interferometers and DBRs via Layer-by-Layer Nanoassembly (Experimental Section), and a time-resolved sensorgram is shown in Figure S4a. Figure 2a reports reflectance spectra of an oxidized PSi interferometer, recorded in DIW before and after coating with PAH and after decoration with AuNPs. A clear decrease of the reflectance intensity between 400 and 600 nm occurred after AuNP decoration, which corresponded to localized surface plasmon resonance of the 15 nm AuNPs (compare with LSPR spectrum of AuNP dispersion in water reported in Figure S3). Further, an increase of the interferometric Fabry−Pérot fringe contrast after adsorption of AuNPs on the PSi skeleton was apparent. Accordingly, the FFT amplitude showed a ∼(3.7 ± 1.2)-fold increase after decoration with AuNPs, due to the contrast increase in the Fabry−Pérot fringes (Figure 2b).

EOT analysis of the experimental reflectance spectra showed that the EOT values obtained after assembling of PAH and anchoring of AuNPs increased (20.4 ± 8.1 nm) and then decreased (−113 ± 39 nm), respectively, compared to the reference EOT value of oxidized PSi interferometers in DIW (Figure S4a,b), in agreement with data recorded in air (Figure 1c).

Different concentrations of NaCl in deionized water (i.e., 1, 2, 5, and 10% (w/v), corresponding to a refractive index

DOI: 10.1021/acsami.9b15737
ACS Appl. Mater. Interfaces XXXX, XXX, XXX−XXX

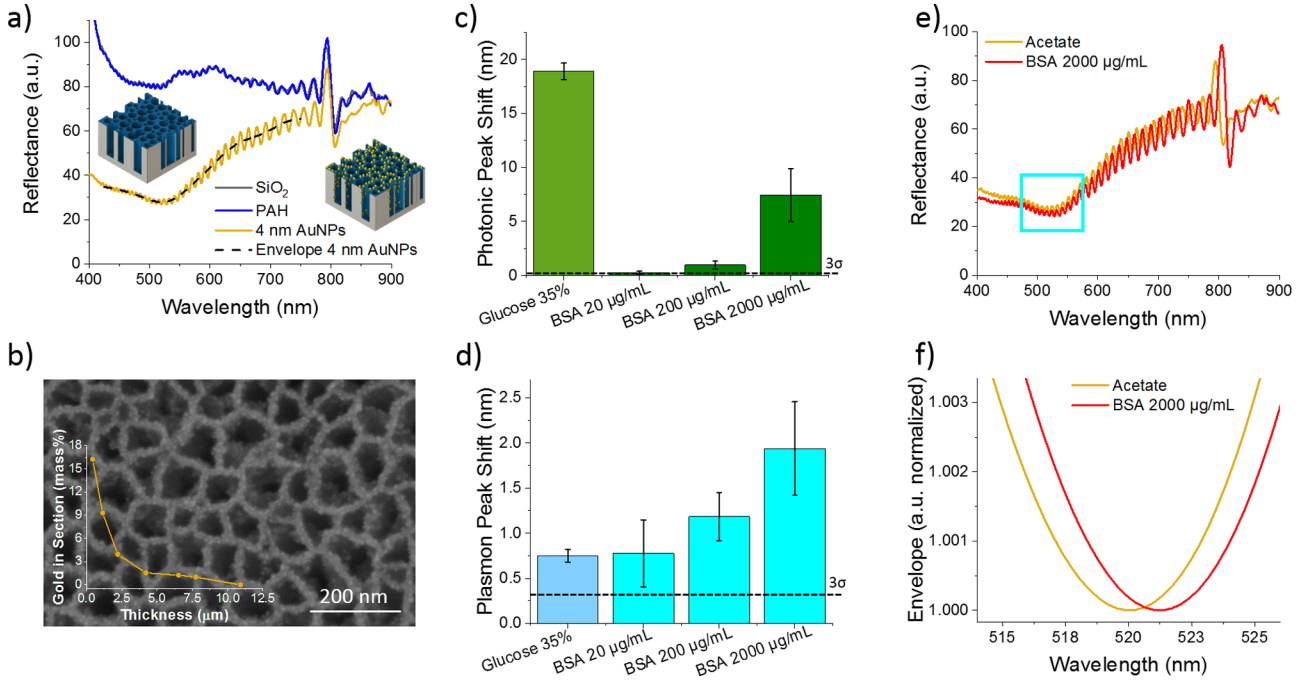

Figure 3. Hybrid photonic–plasmonic AuNPs-PSi DBR (bio)sensor characterization. (a) Reflectance spectra of an oxidized PSi DBR acquired in DIW, before (gray)and after (blue) PAH coating and after decoration with 4 nm sized AuNPs (yellow). (b) Top-view SEM image of a PAH-coated PSi DBR decorated with 4 nm sized AuNPs. Inset: AuNP mass percentage along the depth of the decorated PSi DBR. (c, d) Shifts of the photonic peak and of the envelope of the plasmonic absorption peak after injection of a 35% glucose solution and upon unspecific adsorption of BSA (20, 200, and 2000 μg/mL). (e) Reflectance spectra (au) of the AuNPs–decorated PSi DBR acquired in acetate buffer before and after unspecific adsorption of BSA (2000 μg/mL). (f) Zoom from panel (e) showing the shift of the envelope of the plasmon absorption peak. Data in panels (c) and (d) are provided as average values over three replicates, with error bars representing one standard deviation. The dashed lines depict three times the noise floor of the photonic and plasmonic peak positions in acetate buffer before BSA infiltration (i.e., 0.39 and 0.33 nm, respectively).

variation of 0.6×10^{-3}, 1.2×10^{-3}, 3.0×10^{-3}, and 6.0×10^{-3} RIU, compared to deionized water, respectively) were infiltrated both in nondecorated and AuNPs-decorated interferometers, and the IAW − IAW_0 signal was measured over time (using the IAW_0 value in DIW as reference). In Figure 2c sensorgrams for both nondecorated and decorated PSi interferometers are reported, from which it is evident that higher IAW values were recorded for the AuNPs-decorated interferometer.

In Figure 2d we report the calibration curves achieved for the two PSi interferometers in Figure 1c at the different NaCl concentrations injected, that is, IAW − IAW_0 vs refractive index variations (Δn). The experimental points were best-fitted with a linear function, namely, IAW − IAW_0 = $144\Delta n$ and IAW − IAW_0 = $642\Delta n$ for nondecorated and decorated interferometers, respectively. The slope of the linear regression curves represents the sensitivity of the two interferometers for bulk refractive index variations, proving that a ∼4.5-fold increase on sensitivity was achieved upon decoration with AuNPs. Theoretical limit of detection (LoD) was calculated from the linear calibration curve by extrapolation of the refractive index variation value at which the IAW − IAW_0 value is equal to $3\sigma_{IAW_0}$ = 0.004 au (i.e., signal-to-noise ratio SNR = 3), σ_{IAW_0} being the noise floor (i.e., standard deviation of IAW_0) in DIW. As a result, an LoD value of 2.8×10^{-5} and 6.2×10^{-6} RIU was achieved for nondecorated and AuNPs-decorated interferometers, respectively. This represents a 4.5-fold improvement, pushing the LoD of Au-decorated PSi interferometers down to that of "gold standard" optical label-free platforms, namely, surface plasmon resonance with LoD in the range of 10^{-6} RIU.[54]

Such an AuNPs-mediated signal enhancing was also evaluated for perspective biosensing applications, monitoring both BSA unspecific adsorption and biotin/streptavidin affinity binding on nondecorated and AuNPs-decorated PSi interferometers. The BSA unspecific adsorption has been often employed in the literature as a model for proof-of-concept studies of perspective biosensing applications.[52,53] A BSA solution with concentration of 1000 μg/mL was prepared in acetate buffer, and the buffer pH was tuned to the BSA isoelectric point (pI ∼ 4.7) to maximize its diffusion inside the nanopores.[52] The sensorgrams recorded for the two interferometers (Figure S5) and the related IAW − IAW_0 signals (Figure 2e) prove that a ∼2.6-fold increase was achieved for the AuNPs-decorated interferometer (5.39 ± 0.41 au), compared to the nondecorated one (2.04 ± 0.32 au). In addition, the sensorgram in Figure S5 shows that such an enhancing occurred without affecting the diffusion kinetics of biomolecules (e.g., BSA) inside the decorated nanopores.

Further, specific streptavidin (STV, 500 μg/mL) binding to a biotinylated poly(methacrylic acid) (b-PMAA, negatively charged) assembled on PAH-coated interferometers without and with AuNP decoration was verified. Figure 2f shows time-resolved EOT − EOT_{AuNPs} signal demonstrating the successful b-PMAA assembly on AuNPs-decorated interferometers. Analogously to BSA, STV was solubilized in acetate buffer and the buffer pH was tuned to the protein isoelectric point (pI ∼ 5) to maximize its diffusion inside the nanopores and, in turn, binding to b-PMAA.[52] Selectivity of the affinity interaction between STV and b-PMAA was ensured by a

DOI: 10.1021/acsami.9b15737
ACS Appl. Mater. Interfaces XXXX, XXX, XXX–XXX

repulsive rinsing step in HEPES buffer at pH 7.4, carried out after STV injection, according to the protocol described in the Injection Protocols (Experimental Section) and previously reported by our group.[15] Rinsing in HEPES at pH = 7.4, which is higher than the isoelectric point (pI = 5) of STV, yielded STV negatively charged (i.e., with the same polarity of PMAA polymer), thus promoting electrical repulsion and desorption of STV nonspecifically bound to b−PMAA.[15] The AuNP decoration led to a significant ∼2.5-fold increase of the recorded IAW − IAW_0 signals (1.88 ± 0.45 au) for the selective binding between STV and b-PMAA, compared to nondecorated PSi interferometer (i.e., 0.77 ± 0.24 au) (Figure 2e). The achieved results prove that the decoration of PSi interferometers with AuNPs led to an increase in binding signals (both unspecific and selective), without restricting the diffusion kinetics of biomolecules (and also polymers, such as, b-PMAA) in nanometric pores with aspect ratio of roughly 50 (average diameter 100 nm and thickness 5 μm).

Hybrid Photonic/Plasmonic AuNPs-PSi Platform for Perspective (Bio)sensing. The reflectance spectra in Figure 1b clearly show that the presence of AuNPs within PSi interferometers resulted in intensity attenuation in the range 400−600 nm ascribable to plasmonic absorption. The plasmonic effect of AuNPs on the PSi interferometer reflectance spectrum was more pronounced for decoration with 4 nm AuNPs, compared to 15 nm ones, which ensured a greater decoration of the nanopores with depth (Figure 1g). Thus, we focused on 4 nm AuNPs for decoration of PSi DBR structures aimed at the realization of a plasmonic/photonic hybrid platform.

PSi DBRs were prepared with a stop-band centered at 656.6 ± 5.3 nm, and consisted of 40 high- and low-porosity bilayers with porosities of 81 and 76%, respectively, for a total thickness of 11.5 μm. Before decoration with AuNPs the PSi DBR was subjected to thermal oxidation. Reflectance spectra of as-prepared and oxidized PSi DBR are shown in Figure S6. The oxidation of the PSi skeleton led to blue shift (−29.2 ± 3.9 nm) and intensity attenuation of the photonic bandgap, due to conversion of silicon to silicon dioxide. Then, the oxidized PSi DBR was secured into a flow cell, and a PAH layer was assembled by LbL onto the nanopore surface generating a red shift (1.5 ± 0.4 nm) of the photonic bandgap (compared to its position before PAH coating). Decoration of the PAH-coated PSi DBR with 4 nm AuNPs was then carried out (in the flow cell), leading to a significant decrease of the reflectance intensity in the region of 400−600 nm, ascribable to LSPR of the AuNPs, with negligible effect on the photonic bandgap (Figure 3a).

Figure 3b shows a top-view SEM image of a PSi DBR decorated with 4 nm AuNPs, confirming decoration of the PSi skeleton with AuNPs. The EDS analysis of the cross-section revealed that the 4 nm AuNPs efficiently decorated the inner surface of PSi DBR over the whole thickness with a decaying profile, with an Au mass of 16.5% on top, reducing toroughly 1.5% at half-thickness (∼6 μm).

Wavelength positions of both photonic bandgap peak and plasmonic absorption peak (upon extraction of the envelop as described in Photonic and Plasmonic Peak Tracking for (Bio)sensing Measurement with AuNPs-Decorated PSi DBRs, Experimental Section) were simultaneously tracked for the characterization of the hybrid DBR in (bio)sensing applications. Specifically, to investigate the sensitivity of the hybrid DBR to bulk refractive index variation, a 35% glucose solution in DIW was injected in the flow cell ($\Delta n = 5.1 \times 10^{-2}$ RIU, compared to DIW), and the simultaneous shifts of photonic and plasmonic peaks were monitored (Figure S7).

Wavelength changes ($\Delta\lambda$) of both photonic and plasmonic peaks were observed (Figure 3c,d), namely, 19.9 ± 0.8 and 0.75 ± 0.07 nm, respectively, resulting in a sensitivity to bulk refractive index variation of 408 and 14.7 nm/RIU, respectively, calculated considering the linear dependence of refractive index on glucose concentration.[55] The sensitivity of the plasmonic peak resulted in a 27-fold lower value than that of the photonic stop-band, in agreement with the lower LSPR sensitivity measured for 4 nm AuNP dispersion with the same 35% glucose solution (Figure S8; $\Delta\lambda$ = 3.97 nm; sensitivity ∼78 nm/RIU). The lower sensitivity of AuNPs anchored to the PSi DBR surface, with respect to that of the AuNP dispersion, can be explained in terms of a reduced degree of freedom of the particles and lower surface exposed to the glucose solution once assembled on a solid surface.[17] The results achieved agree well with data reported by Budy et al.[17] on the sensitivity of LbL nanoassembly of gold nanospheres (20 nm diameter, citrate-capped) on a glass substrate for LSPR refractive index measurements with sucrose solutions. The authors reported sensitivities of 18.8 nm/RIU for AuNPs anchored onto the glass surface and 71.6 nm/RIU for AuNPs in colloidal dispersion.[17]

For perspective biosensing applications, we evaluated BSA unspecific adsorption on the hybrid plasmonic/photonic DBR. BSA solutions with concentrations of 20, 200, and 2000 μg/mL were prepared in acetate buffer, and the buffer pH was tuned to the BSA isoelectric point (pI ∼ 4.7) to maximize its diffusion inside the nanopores.[52]

The shift of photonic (i.e., 0.24 ± 0.16, 0.98 ± 36, and 7.4 ± 2.4 nm) and plasmonic (i.e., 0.78 ± 0.37, 1.18 ± 0.27, and 1.94 ± 0.52 nm) peaks acquired for the three tested BSA concentrations are summarized in Figure 3c,d. Taking into account three times the noise floor, i.e., $3\sigma_0$ = 0.39 and 0.33 nm for photonic and plasmonic peak positions, respectively, with σ_0 standard deviation in acetate buffer before BSA infiltration, all of the achieved signals were significant except for the photonic peak shift at 20 μg/mL BSA.

Panels (e) and (f) of Figure 3 report the reflectance spectra of an AuNPs-PSi DBR acquired in acetate buffer before and after injection of 2000 μg/mL BSA. Shift of both photonic (Figure 3e) and plasmonic (Figure 3e,f) peaks are apparent upon adsorption of BSA on the PSi DBR coated with AuNPs, thus proving that hybrid photonic/plasmonic platforms can be effectively designed for future (bio)sensing applications.

To the best of our knowledge, this is the first evidence of a hybrid photonic/plasmonic PSi DBR for sensing and perspective biosensing applications.

CONCLUSIONS

In this work, LbL nanoassembly of citrate-capped spherical gold nanoparticles (AuNPs, negatively charged, with diameters of 15 and 4 nm) and positively charged polyelectrolyte (i.e., PAH) was successfully demonstrated as a robust and effective route for the decoration of PSi nanostructured interferometers and DBRs for (bio)sensing applications.

We found that the 15 nm AuNPs poorly penetrated into the inner surface of PSi interferometers, so that the decoration occurred mainly on the top of the PSi surface. This provided an increase of Fabry−Pérot fringes (∼3.3-fold) ascribable to the increase in reflectivity of the top interface, due to the slight

DOI: 10.1021/acsami.9b15737
ACS Appl. Mater. Interfaces XXXX, XXX, XXX−XXX

metallization of the surface and the subsequent mirroring effect.[43] This resulted in an interferometric augmented sensitivity for both bulk refractive index sensing (roughly 4.5-fold) and surface refractive index sensing (about 2.5-fold for unspecific adsorption of BSA and affinity biosensing of streptavidin).

On the other hand, the 4 nm AuNPs enabled the decoration of the inner surface of PSi DBRs, allowing one to build up a photonic/plasmonic optical sensing platform. Both photonic (DBR stop-band) and plasmonic (LSPR) peaks were shown to be sensitive to changes of bulk refractive index. The achieved sensitivities of the photonic and plasmonic peaks were 408 and 14.7 nm/RIU, respectively. The sensitivity of the plasmonic peak was in good agreement with results reported by Budy et al.[17] about the sensitivity of a LbL nanoassembly of gold nanospheres on a glass substrate (i.e., 18.8 nm/RIU).[17] The hybrid photonic/plasmonic platform was also proved to be sensitive to BSA unspecific adsorption, used as a proof-of-concept of perspective biosensing applications.

We believe that by building on these results, hybrid PSi-AuNP (bio)sensing platforms with superior performance could be achieved, leveraging the design of AuNPs with specific size and morphology[56] to boost the interferometric signal and/or photonic/plasmonic sensitivity.

EXPERIMENTAL SECTION

Materials and Chemicals. Boron-doped (p-type) silicon wafers, resistivity of 0.8−1.2 mΩ·cm and orientation ⟨100⟩, were purchased from Sil'tronix Silicon Technologies (France). Aqueous hydrofluoric acid (HF, 48%) and tetrachloroauric(III) acid trihydrate ($HAuCl_4 \cdot 3H_2O$, 99%) were purchased from Merck Millipore (Germany). Absolute ethanol (EtOH, 99.9%) and diethyl ether (Et_2O, 99,7%) were purchased from Carlo Erba Reagents (Italy). Poly(allylamine hydrochloride) (PAH, 40000 Da) was purchased from Beckmann-Kenko (Germany). Poly(methacrylic acid) (PMAA) was purchased from Polysciences (Germany), and it was biotinylated (b-PMAA) according to the protocol reported in ref 15. Sodium chloride (NaCl, 99.5%), sodium citrate (Na_3Ct, 99%), sodium borohydride ($NaBH_4$, 96%), sodium acetate (CH_3COONa, 99%), acetic acid (CH_3COOH, 99%), 4-(2-hydroxyethyl)-1-piperazineethanesulfonic acid (HEPES, 99.5%), sodium hydroxide (NaOH, 97%), hydrochloridric acid (HCl, 37%), bovine serum albumin (BSA, ≥98%, pI = 4.7, MW = 66430 Da), and streptavidin from *Streptomyces avidinii* (STV, pI = 5.0, MW = 60 kDa) to be used for affinity biosensing were purchased from Sigma-Aldrich (Milan, Italy).

Aqueous buffers and solutions were prepared using deionized water purified by Elix (Merck Millipore, Germany), filtered using syringe filters (Minisart NML Syringe Filters 1.20 μm, Sartorius, Germany) and pH-adjusted with NaOH (5 M) and HCl (1 M) aqueous solution.

Preparation of Porous Silicon Interferometers and Distributed Bragg Reflectors. Porous silicon samples (interferometers and distributed Bragg reflectors, DBRs) were prepared by anodic etching of p-type silicon square wafer samples (1.5 × 1.5 cm^2) using a solution of HF(48%):EtOH, 3:1 (v/v). ***Caution!*** *HF is a highly corrosive acid, and it has to be handled with extreme care under safe work conditions!* Silicon wafers were placed in a Teflon cell with platinum wire cathode and flat aluminum anode, and the etching was driven by a Keithley 2602A source measurement unit.

First, a sacrificial PSi layer was etched at a current density of 700 mA/cm^2 for 10 s and dissolved in NaOH(1M):EtOH, 9:1 (v/v), to avoid the presence of a parasitic layer restricting the diffusion of biomolecules in PSi underneath. After dissolution of the sacrificial PSi layer, the samples were rinsed in DIW and gently dried under nitrogen flow, then etching of a PSi optical component, either an interferometer or a DBR, was carried out.

PSi interferometers were etched with a constant current density of 700 mA/cm^2 for 23 s, in order to obtain a layer with thickness of about 5 μm and porosity of about 80%.

PSi DBRs were etched with a square-wave etching current density consisting of alternating high 700 mA/cm^2 for 0.71 s (porosity of 81% and thickness of 146 nm) and low 400 mA/cm^2 for 0.91 s (porosity of 76% and thickness of 143 nm) current density values for a total of 40 cycles, in order to obtain an optical filter with thickness of about 11.5 μm and photonic bandgap centered at 650 nm.

The prepared PSi samples were then rinsed with ethanol and diethyl ether and gently dried under nitrogen flow to obtain a crack-free PSi layer.

Eventually, PSi samples were thermally oxidized in a muffle furnace (ZB 1, ASAL) at 750 °C for 1 h, with a ramp rate of 12 °C/min, in ambient atmosphere.

Gold Nanoparticle Synthesis Protocols and Optical Characterization. Citrate-capped spherical gold nanoparticles (AuNPs) with different diameters (i.e., 15 and 4 nm) were synthesized for porous silicon decoration via layer-by-layer nanoassembly.

AuNPs with 15 nm diameter were synthesized accordingly to the Turkevich method.[40] The synthesis was based on sodium citrate ($[Na_3Ct]$ = 0.875 mM) mediated reduction of tetrachloroauric(III) acid ($[HAuCl_4]$ = 0.25 mM; molar ratio = $[Na_3Ct]/[HAuCl_4]$ = 3.5) in deionized water solution at 100 °C for 10 min under magnetic stirring.[41]

AuNPs with 4 nm diameter were synthesized according to the method reported by Haiss et al.[42] The synthesis was based on sodium borohydride ($[NaBH_4]$ = 19.8 mM) mediated chemical reduction of tetrachloroauric(III) acid ($[HAuCl_4]$ = 0.27 mM) in a deionized water solution with sodium citrate ($[Na_3Ct]$ = 0.83 mM) at room temperature under magnetic stirring for 5 min.

The absorbance spectra of the AuNP dispersions were collected with an Ocean Optics HR4000 spectrometer in combination with a fiber-coupled Ocean Optics DH-2000 deuterium−halogen light source and a glass cuvette (Optical special glass, 12.5 × 45 mm; path length, 10 mm; Hellma, Germany). Size and concentration of the AuNPs were estimated by the absorbance spectra of AuNPs reported in Figure S3, in accord with the method reported by Haiss et al.[42] The resulting 15 and the 4 nm sized AuNPs dispersions had estimated concentrations of 2.84×10^{-9} and 4.20×10^{-7} M, respectively.

AuNPs-Decoration of Porous Silicon Interferometers and DBRs via Layer-by-Layer Nanoassembly. For SEM and EDS analysis, batch decoration of PSi interferometers was carried out. Oxidized porous silicon interferometers were LbL-coated with PAH (1 mg/mL in 50 mM acetate buffer with 200 mM NaCl at pH 5.6), which is a positively charged polyelectrolyte, exploiting electrostatic attraction with the negatively charged oxidized surface of PSi interferometers. The PAH solution (100 μL) was drop-cast onto the oxidized PSi interferometers and left incubating for 2 h at room temperature to ensure full infiltration of the nanopores of the PSi layer. The interferometers were then abundantly rinsed with DIW and ethanol and gently dried under a nitrogen flow. The PAH-coated porous silicon interferometers were then immersed in 2 mL of a citrate-capped AuNP dispersion (with 15 or 4 nm sized nanoparticles) and left incubating for 14 h for AuNP electrostatic anchoring on the positively charged PAH. The interferometers were then abundantly rinsed with DIW and gently dried under a nitrogen flow.

For (bio)sensing experiments, in-flow decoration of oxidized PSi interferometers and DBRs was carried out. The samples were mounted in the flow cell of an optofluidic setup previously described by our group.[19] A volume of 200 μL of a PAH solution (1 mg/mL in 50 mM acetate buffer with 200 mM NaCl at pH 5.6) was injected in the flow cell at a flow rate of 2 μL/min for 100 min. An abundant rinse with DIW at 100 ul/min was carried out to remove unanchored PAH and confirm PAH coating of the inner oxidized PSi structure.

A citrate-capped AuNP dispersion with 15 or 4 nm sized nanoparticles was injected in the flow cell containing the PAH-coated interferometer or DBR, respectively, at a flow rate of 2 μL/min until saturation of the output signal, namely, $EOT - EOT_0$, occurred (see Fast Fourier Transform Reflectance Spectroscopy, Experimental

DOI: 10.1021/acsami.9b15737
ACS Appl. Mater. Interfaces XXXX, XXX, XXX−XXX

Section). An abundant rinse with DIW at 100 μL/min was carried out to remove AuNP excess and confirm the anchoring of AuNPs on the PAH polyelectrolyte.

Similarly, biotinylated PMAA (b-PMAA, 1 mg/mL in 50 mM acetate buffer with 200 mM NaCl at pH 5.6) was injected in the flow cell containing the AuNPs-decorated PSi interferometer and DBR, at a flow rate of 2 μL/min for 100 min, followed by an abundant rinse with DIW at 100 μL/min.

Morphological, Compositional, and Optical Characterization of PSi Interferometers and DBRs before and after AuNP Decoration. Morphological and compositional characterization of PSi interferometers and DBRs were both carried out using a scanning electron microscope (FE-SEM, FEI Quanta 450 ESEM FEG) equipped with an energy-dispersive microanalytic system (EDS, Bruker, QUANTAX XFlash Detector 6|10 for EDS analysis). SEM and EDS analysis was performed on top and sections of samples with a 15 kV acceleration voltage at various magnifications. Porosity of the layers was evaluated by best-fitting of experimental reflection spectra of as-prepared PSi samples with a homemade Matlab software (MathWorks, USA).[30]

Both as-prepared and thermally oxidized PSi layers were optically characterized in air in the wavelength range of 400−1000 nm using a fiber-optic setup consisting of a halogen lamp source (HL-2000), a bifurcated fiber-optic probe (QR200-7-VIS-BX), and a UV−vis spectrometer (USB2000+VIS-NIR-ES) purchased from Ocean Optics (USA). Light exiting from the halogen lamp source was fed through one arm of the bifurcated fiber-optic probe orthogonally onto the PSi surface, and the reflected light was collected through the other arm of the bifurcated fiber-optic probe into the spectrometer that yields the reflection spectra. Acquisition parameters of reflection spectra were: integration time of 2 ms, average scan number 5, and boxcar width 5; the measured spectra were normalized with respect to a reference mirror (protected silver mirror, Thorlabs, USA).

Fast Fourier Transform Reflectance Spectroscopy. Optical characterization of the PSi layer through fast Fourier transform reflectance spectroscopy (FFT-RS) was used to monitor changes in the effective optical thickness (EOT) = $2n_{eff}d$, where n_{eff} is the effective refractive index and d is the thickness of the PSi layer.

FFT analysis of the reflectance spectra of PSi interferometers was performed using homemade Matlab software. First, the wavelength axis of the reflectance spectrum was inverted (x axis changed from wavelength to 1/wavelength) to obtain a wavenumber axis. A cubic-spline interpolation of reflectance data was then carried out to obtain an evenly spaced (sample-to-sample distance 6.77×10^{-7} nm^{-1}) reflection−wavenumber data set. A Hann window was applied to the reflectance spectrum, and eventually the FFT algorithm was applied to the zero-padded (up to 2^{24} samples) reflectance spectrum, yielding a resolution of about 0.07 nm. The EOT value was obtained as the value of the 1/wavenumber axis (x axis of the Fourier transform domain) for which the maximum peak in the Fourier transform amplitude (y axis) occurs.

Interferogram Average over Wavelength Reflectance Spectroscopy for (Bio)sensing Measurements with AuNPs-Decorated PSi Interferometers. The IAW reflectance spectroscopy[53] was used to monitor the refractive index variation due to the infiltration of NaCl solutions (1, 2, 5, and 10% (w/v)) in deionized water, the unspecific adsorption of 1000 μg/mL BSA, and the selective 500 μg/mL streptavidin biosensing both on AuNPs-decorated and nondecorated PSi interferometers.

Spectral interferograms were calculated by subtraction (wavelength by wavelength) of the reflectance spectrum acquired after each injection from the reference reflectance spectrum acquired in the running buffer (i.e., DIW, acetate buffer). Each interferogram was then corrected for its average value, which was subtracted from the interferogram. Eventually, the output signal, namely, IAW, was obtained by application of the absolute value function to each so-processed interferogram and subsequent calculation of the average value of the resulting interferogram over the spectral range of interest [500−800 nm]. An interferogram was used as the baseline for subsequent IAW measurement, calculated for the running buffer (namely, blank interferogram) by subtraction of the reflectance spectrum acquired in acetate buffer before starting to inject the BSA solutions (IAW_0).

Photonic and Plasmonic Peak Tracking for (Bio)sensing Measurements with AuNPs-Decorated PSi DBRs. Tracking of photonic and plasmonic peaks was used to monitor refractive index variations induced by infiltration of a glucose aqueous solution (35% (w/v)) and unspecific adsorption of BSA (20, 200, and 2000 μg/mL) inside the nanopores of AuNPs-decorated DBRs. For plasmonic peak tacking, an envelope of the plasmon resonance in the wavelength range 400−600 nm was extracted using a low pass filter (Butterworth eighth order; 0.015 nm^{-1} cutoff frequency) in Matlab environment.

Theoretical Spectra Calculation. Theoretical spectra were estimated using the transfer matrix method (TMM) and Bruggemann's equivalent medium approximation.[43] Namely, a complex and dispersive refractive index of each layer was calculated using N-components Bruggemann's equation iteratively solved using the Newton method; then the dispersive transfer matrix of each layer was calculated, and the obtained equivalent matrix of the stacked structure was used to estimate the wavelength-dependent reflectance. All of the calculations were done with a homemade Matlab program considering a PSi layer of 5 μm with 80% porosity, which became roughly 50% after full oxidation. For theoretical spectra calculation after AuNPs' assembly only on the top of the PSi skeleton, a hexagonally arranged layer of spherical Au nanoparticles on top was considered (volume fill factor = $\pi/(3\sqrt{3})$). For theoretical spectra calculation after AuNP assembly only inside the PSi skeleton, a gradient pattern with depth reflecting that achieved with SEM-EDS measurements was considered.

Injection Protocols. NaCl (1, 2, 5, and 10% (w/v)) and glucose (35% (w/v)) aqueous solutions for refractive index sensing measurements were injected starting from deionized water at a flow rate of 20 μL/min for 10 min.

BSA and STV solutions were injected starting from acetate buffer at a flow rate of 5 μL/min for 40/50 min, and then rinsed at 100 μL/min until signal stability ($IAW - IAW_0$ or $\Delta\lambda$, for interferometers and DBRs, respectively). For STV, an additional repulsive rinse step with HEPES buffer was performed at a flow rate of 100 μL/min for 20-30 min, in order to desorb STV nonspecifically adsorbed on b-PMAA. Eventually, acetate buffer was re-injected in the flow cell and the flow rate lowered to 5 μL/min.

Calculation of the Refractive Index of NaCl and Glucose Solutions. The refractive index variations (Δn, compared to that of deionized water) of 1, 2, 5, and 10% (w/v) NaCl aqueous solutions, namely, 6.0×10^{-4}, 1.2×10^{-3}, 3.0×10^{-3}, and 6.0×10^{-3}RIU, were previously calculated using the Lorentz−Lorenz media approximation.[19]

The refractive index variation of 35% (w/v) glucose aqueous solution, namely, 5.1×10^{-2} RIU, was estimated by the refractive index increment value (0.145 cm^3/g) reported in the literature.[57]

■ ASSOCIATED CONTENT

Supporting Information

The Supporting Information is available free of charge on the ACS Publications website at DOI: 10.1021/acsami.9b15737.

PSi reflectance spectra; simulation of reflectance spectra; sensorgrams; DBR reflectance spectra; reflectance spectra; LSPR absorbance spectra (PDF)

■ AUTHOR INFORMATION

Corresponding Author

*E-mail: g.barillaro@iet.unipi.it.

ORCID

Giuseppe Barillaro: 0000-0001-6197-4851

Author Contributions

G.B. and S.M. contributed to the design of the study. S.M. and A.P. carried out the experiments and collected the data, which

DOI: 10.1021/acsami.9b15737
ACS Appl. Mater. Interfaces XXXX, XXX, XXX−XXX

were analyzed and interpreted in conjunction with G.B., S.M., A.P., and A.A.L.M. S.M. and G.B. wrote the manuscript, all authors were involved in revisions, and A.D. prepared, characterized, and engineered the polyelectrolytes, under L.D.'s supervision. G.B. supervised the research work.

Funding

This work was jointly supported by the EU H2020 ETN SYNCHRONICS under Grant Agreement 643238 and by the Italian Minister for University and Research (MIUR) Futuro in Ricerca (FIR) program under Grant No. RBFR122 KL1 (SENS4BIO).

Notes

The authors declare no competing financial interest.

■ ACKNOWLEDGMENTS

S.M. and G.B. thank Rosamaria Corsaro for helping with sample fabrication during her master thesis at the University of Pisa.

■ ABBREVIATIONS

AuNPs, gold nanoparticles
AuNPLs, gold nanoparticle layers
b-PMAA, biotinylated poly(methacrylic acid) (b-PMAA)
BSA, bovine serum albumin
DBRs, distributed Bragg reflectors
DIW, deionized water
ELISA, enzyme-linked immunosorbent assay
EOT, effective optical thickness
FFT, fast Fourier transform
IAW, interferogram average over wavelength
LbL, layer by layer
(L)SPR, (localized) surface plasmon resonance
LoD, limit of detection
PAH, poly(allylamine hydrochloride)
PSi, porous silicon
RIU, refractive index unit
SEM-EDS, scanning electron microscopy−energy-dispersive X-ray spectroscopy
SERS, surface enhanced Raman scattering
STV, streptavidin
TMM, transfer matrix method

■ REFERENCES

(1) Wu, J.; Qu, Y.; Yu, Q.; Chen, H. Gold Nanoparticle Layer: A Versatile Nanostructured Platform for Biomedical Applications. *Mater. Chem. Front.* **2018**, *2* (12), 2175−2190.
(2) Estevez, M.-C.; Otte, M. a; Sepulveda, B.; Lechuga, L. M. Trends and Challenges of Refractometric Nanoplasmonic Biosensors: A Review. *Anal. Chim. Acta* **2014**, *806*, 55−73.
(3) Mariani, S.; Ermini, M. L.; Scarano, S.; Bellissima, F.; Bonini, M.; Berti, D.; Minunni, M. Improving Surface Plasmon Resonance Imaging of DNA by Creating New Gold and Silver Based Surface Nanostructures. *Microchim. Acta* **2013**, *180* (11), 1093−1099.
(4) Abraham, S.; König, M.; Srivastava, S. K.; Kumar, V.; Walkenfort, B.; Srivastava, A. Carbon Nanostructure (0−3 Dimensional) Supported Isolated Gold Nanoparticles as an Effective SERS Substrate. *Sens. Actuators, B* **2018**, *273*, 455−465.
(5) Kho, K. W.; Shen, Z. X.; Zeng, H. C.; Soo, K. C.; Olivo, M. Deposition Method for Preparing SERS-Active Gold Nanoparticle Substrates. *Anal. Chem.* **2005**, *77* (22), 7462−7471.
(6) Lai, C.-H.; Wang, G.-A.; Ling, T.-K.; Wang, T.-J.; Chiu, P.; Chou Chau, Y.-F.; Huang, C.-C.; Chiang, H.-P. Near Infrared Surface-Enhanced Raman Scattering Based on Star-Shaped Gold/Silver Nanoparticles and Hyperbolic Metamaterial. *Sci. Rep.* **2017**, *7* (1), 5446.
(7) Toh, S. Y.; Citartan, M.; Gopinath, S. C. B.; Tang, T.-H. Aptamers as a Replacement for Antibodies in Enzyme-Linked Immunosorbent Assay. *Biosens. Bioelectron.* **2015**, *64*, 392−403.
(8) Zhou, F.; Yuan, L.; Wang, H.; Li, D.; Chen, H. Gold Nanoparticle Layer: A Promising Platform for Ultra-Sensitive Cancer Detection. *Langmuir* **2011**, *27* (6), 2155−2158.
(9) Zhou, F.; Wang, M.; Yuan, L.; Cheng, Z.; Wu, Z.; Chen, H. Sensitive Sandwich ELISA Based on a Gold Nanoparticle Layer for Cancer Detection. *Analyst* **2012**, *137* (8), 1779−1784.
(10) Pingarrón, J. M.; Yáñez-Sedeño, P.; González-Cortés, A. Gold Nanoparticle-Based Electrochemical Biosensors. *Electrochim. Acta* **2008**, *53* (19), 5848−5866.
(11) Jeong, H.-H.; Choi, E.; Ellis, E.; Lee, T.-C. Recent Advances in Gold Nanoparticles for Biomedical Applications: From Hybrid Structures to Multi-Functionality. *J. Mater. Chem. B* **2019**, *7* (22), 3480−3496.
(12) Saha, K.; Agasti, S. S.; Kim, C.; Li, X.; Rotello, V. M. Gold Nanoparticles in Chemical and Biological Sensing. *Chem. Rev.* **2012**, *112* (5), 2739−2779.
(13) Mohanty, U. S. Electrodeposition: A Versatile and Inexpensive Tool for the Synthesis of Nanoparticles, Nanorods, Nanowires, and Nanoclusters of Metals. *J. Appl. Electrochem.* **2011**, *41* (3), 257−270.
(14) Decher, G. Fuzzy Nanoassemblies: Toward Layered Polymeric Multicomposites. *Science* **1997**, *277* (5330), 1232−1237.
(15) Mariani, S.; Robbiano, V.; Strambini, L. M.; Debrassi, A.; Egri, G.; Dähne, L.; Barillaro, G. Layer-by-Layer Biofunctionalization of Nanostructured Porous Silicon for High-Sensitivity and High-Selectivity Label-Free Affinity Biosensing. *Nat. Commun.* **2018**, *9* (1), 5256.
(16) Richardson, J. J.; Cui, J.; Björnmalm, M.; Braunger, J. A.; Ejima, H.; Caruso, F. Innovation in Layer-by-Layer Assembly. *Chem. Rev.* **2016**, *116* (23), 14828−14867.
(17) Budy, S. M.; Hamilton, D. J.; Cai, Y.; Knowles, M. K.; Reed, S. M. Polymer Mediated Layer-by-Layer Assembly of Different Shaped Gold Nanoparticles. *J. Colloid Interface Sci.* **2017**, *487*, 336−347.
(18) Anderson, M. A.; Tinsley-Bown, A.; Allcock, P.; Perkins, E. A.; Snow, P.; Hollings, M.; Smith, R. G.; Reeves, C.; Squirrell, D. J.; Nicklin, S.; Cox, T. I. Sensitivity of the Optical Properties of Porous Silicon Layers to the Refractive Index of Liquid in the Pores. *Phys. Status Solidi* **2003**, *197* (2), 528−533.
(19) Mariani, S.; Strambini, L. M.; Barillaro, G. Electrical Double Layer-Induced Ion Surface Accumulation for Ultrasensitive Refractive Index Sensing with Nanostructured Porous Silicon Interferometers. *ACSSensors* **2018**, *3*, 595−605.
(20) Ocier, C. R.; Krueger, N. A.; Zhou, W.; Braun, P. V. Tunable Visibly Transparent Optics Derived from Porous Silicon. *ACS Photonics* **2017**, *4* (4), 909−914.
(21) Pavesi, L.; Dubos, P. Random Porous Silicon Multilayers: Application to Distributed Bragg Reflectors and Interferential Fabry - Pérot Filters. *Semicond. Sci. Technol.* **1997**, *12* (5), 570−575.
(22) Lorenzo, E.; Oton, C. J.; Capuj, N. E.; Ghulinyan, M.; Navarro-Urrios, D.; Gaburro, Z.; Pavesi, L. PorousSilicon-Based Rugate Filters. *Appl. Opt.* **2005**, *44* (26), 5415−5421.
(23) Salem, M. S.; Sailor, M. J.; Fukami, K.; Sakka, T.; Ogata, Y. H. Sensitivity of Porous Silicon Rugate Filters for Chemical Vapor Detection. *J. Appl. Phys.* **2008**, *103* (8), 083516.
(24) Jenie, S. N. A.; Prieto-Simon, B.; Voelcker, N. H. Development of L-Lactate Dehydrogenase Biosensor Based on Porous Silicon Resonant Microcavities as Fluorescence Enhancers. *Biosens. Bioelectron.* **2015**, *74*, 637−643.
(25) Robbiano, V.; Paternò, G. M.; La Mattina, A. A.; Motti, S. G.; Lanzani, G.; Scotognella, F.; Barillaro, G. Room-Temperature Low-Threshold Lasing from Monolithically Integrated Nanostructured Porous Silicon Hybrid Microcavities. *ACS Nano* **2018**, *12* (5), 4536−4544.

DOI: 10.1021/acsami.9b15737
ACS Appl. Mater. Interfaces XXXX, XXX, XXX−XXX

(26) De Stefano, L.; Moretti, L.; Rendina, I.; Rossi, A. M. Porous Silicon Microcavities for Optical Hydrocarbons Detection. *Sens. Actuators, A* **2003**, *104* (2), 179−182.
(27) De Stefano, L.; Moretti, L.; Rendina, I.; Rossi, A. M. Time-Resolved Sensing of Chemical Species in Porous Silicon Optical Microcavity. *Sens. Actuators, B* **2004**, *100* (1), 168−172.
(28) Gao, J.; Gao, T.; Li, Y. Y.; Sailor, M. J. Vapor Sensors Based on Optical Interferometry from Oxidized Microporous Silicon Films. *Langmuir* **2002**, *18* (6), 2229−2233.
(29) Mariani, S.; Strambini, L. M.; Paghi, A.; Barillaro, G. Low-Concentration Ethanol Vapor Sensing With Nanostructured Porous Silicon Interferometers Using Interferogram Average Over Wavelength Reflectance Spectroscopy. *IEEE Sens. J.* **2018**, *18* (19), 7842−7849.
(30) Ruminski, A. M.; Barillaro, G.; Chaffin, C.; Sailor, M. J. Internally Referenced Remote Sensors for HF and Cl2 Using Reactive Porous Silicon Photonic Crystals. *Adv. Funct. Mater.* **2011**, *21* (8), 1511−1525.
(31) Ruminski, A. M.; King, B. H.; Salonen, J.; Snyder, J. L.; Sailor, M. J. Porous Silicon-Based Optical Microsensors for Volatile Organic Analytes: Effect of Surface Chemistry on Stability and Specificity. *Adv. Funct. Mater.* **2010**, *20* (17), 2874−2883.
(32) Arshavsky-Graham, S.; Massad-Ivanir, N.; Segal, E.; Weiss, S. Porous Silicon-Based Photonic Biosensors: Current Status and Emerging Applications. *Anal. Chem.* **2019**, *91* (1), 441−467.
(33) Tieu, T.; Alba, M.; Elnathan, R.; Cifuentes-Rius, A.; Voelcker, N. H. Advances in Porous Silicon−Based Nanomaterials for Diagnostic and Therapeutic Applications. *Adv. Ther.* **2019**, *2* (1), 1800095.
(34) Lin, V. S.-Y.; Motesharei, K.; Dancil, K.-P. S.; Sailor, M. J.; Ghadiri, M. R. A Porous Silicon-Based Optical Interferometric Biosensor. *Science* **1997**, *278* (5339), 840−843.
(35) Vilensky, R.; Bercovici, M.; Segal, E. Oxidized Porous Silicon Nanostructures Enabling Electrokinetic Transport for Enhanced DNA Detection. *Adv. Funct. Mater.* **2015**, *25* (43), 6725−6732.
(36) Mariani, S.; Pino, L.; Strambini, L. M.; Tedeschi, L.; Barillaro, G. 10 000-Fold Improvement in Protein Detection Using Nanostructured Porous Silicon Interferometric Aptasensors. *ACS Sensors* **2016**, *1* (12), 1471−1479.
(37) Zhao, Y.; Gaur, G.; Retterer, S. T.; Laibinis, P. E.; Weiss, S. M. Flow-Through Porous Silicon Membranes for Real-Time Label-Free Biosensing. *Anal. Chem.* **2016**, *88* (22), 10940−10948.
(38) Bandarenka, H. V. SERS Analysis with Porous Silicon. In *Handbook of Porous Silicon*; Canham, L., Ed.; Springer International: Cham, Switzerland, 2016; pp 1−21.
(39) Balderas-Valadez, R. F.; Schürmann, R.; Pacholski, C. One Spot-Two Sensors: Porous Silicon Interferometers in Combination With Gold Nanostructures Showing Localized Surface Plasmon Resonance. *Front. Chem.* **2019**, *7*, 593.
(40) Turkevich, J.; Stevenson, P. C.; Hillier, J. A Study of the Nucleation and Growth Processes in the Synthesis of Colloidal Gold. *Discuss. Faraday Soc.* **1951**, *11* (0), 55−75.
(41) Ji, X.; Song, X.; Li, J.; Bai, Y.; Yang, W.; Peng, X. Size Control of Gold Nanocrystals in Citrate Reduction: The Third Role of Citrate. *J. Am. Chem. Soc.* **2007**, *129* (45), 13939−13948.
(42) Haiss, W.; Thanh, N. T. K.; Aveyard, J.; Fernig, D. G. Determination of Size and Concentration of Gold Nanoparticles from UV-Vis Spectra. *Anal. Chem.* **2007**, *79* (11), 4215−4221.
(43) Born, M.; Wolf, E. *Principles of Optics*; Cambridge University Press: Oxford, U.K., 1999; DOI: 10.1017/CBO9781139644181.
(44) Sailor, M. J. Chemistry of Porous Silicon. *Porous Silicon in Practice*; Wiley-VCH Verlag: Weinheim, Germany, 2011; pp 189−227.
(45) Malitson, I. H. Interspecimen Comparison of the Refractive Index of Fused Silica*,†. *J. Opt. Soc. Am.* **1965**, *55* (10), 1205−1209.
(46) Aspnes, D. E.; Studna, A. A. Dielectric Functions and Optical Parameters of Si, Ge, GaP, GaAs, GaSb, InP, InAs, and InSb from 1.5 to 6.0 EV. *Phys. Rev. B: Condens. Matter Mater. Phys.* **1983**, *27* (2), 985−1009.
(47) Ruths, J.; Essler, F.; Decher, G.; Riegler, H. Polyelectrolytes I: Polyanion/Polycation Multilayers at the Air/Monolayer/Water Interface as Elements for Quantitative Polymer Adsorption Studies and Preparation of Hetero-Superlattices on Solid Surfaces. *Langmuir* **2000**, *16* (23), 8871−8878.
(48) Yakubovsky, D. I.; Arsenin, A. V.; Stebunov, Y. V.; Fedyanin, D. Y.; Volkov, V. S. Optical Constants and Structural Properties of Thin Gold Films. *Opt. Express* **2017**, *25* (21), 25574−25587.
(49) Gao, L.; Lemarchand, F.; Lequime, M. Comparison of Different Dispersion Models for Single Layer Optical Thin Film Index Determination. *Thin Solid Films* **2011**, *520* (1), 501−509.
(50) Ciddor, P. E. Refractive Index of Air: New Equations for the Visible and near Infrared. *Appl. Opt.* **1996**, *35* (9), 1566−1573.
(51) Chegel, V.; Rachkov, O.; Lopatynskyi, A.; Ishihara, S.; Yanchuk, I.; Nemoto, Y.; Hill, J. P.; Ariga, K. Gold Nanoparticles Aggregation: Drastic Effect of Cooperative Functionalities in a Single Molecular Conjugate. *J. Phys. Chem. C* **2012**, *116* (4), 2683−2690.
(52) Chen, M. Y.; Sailor, M. J. Charge-Gated Transport of Proteins in Nanostructured Optical Films of Mesoporous Silica. *Anal. Chem.* **2011**, *83* (18), 7186−7193.
(53) Mariani, S.; Strambini, L. M.; Barillaro, G. Femtomole Detection of Proteins Using a Label-Free Nanostructured Porous Silicon Interferometer for Perspective Ultrasensitive Biosensing. *Anal. Chem.* **2016**, *88* (17), 8502−8509.
(54) Homola, J. Surface Plasmon Resonance Sensors for Detection of Chemical and Biological Species. *Chem. Rev.* **2008**, *108* (2), 462−493.
(55) Fang, Y.-L.; Wang, C.-T.; Chiang, C.-C. A Small U-Shaped Bending-Induced Interference Optical Fiber Sensor for the Measurement of Glucose Solutions. *Sensors* **2016**, *16* (9), 1460.
(56) Chen, H.; Kou, X.; Yang, Z.; Ni, W.; Wang, J. Shape- and Size-Dependent Refractive Index Sensitivity of Gold Nanoparticles. *Langmuir* **2008**, *24*, 5233−5237.
(57) Tumolo, T.; Angnes, L.; Baptista, M. S. Determination of the Refractive Index Increment (Dn/Dc) of Molecule and Macromolecule Solutions by Surface Plasmon Resonance. *Anal. Biochem.* **2004**, *333* (2), 273−279.

DOI: 10.1021/acsami.9b15737
ACS Appl. Mater. Interfaces XXXX, XXX, XXX−XXX